

# Modeling the Excitability of Mammalian Nerve Fibers: Influence of Afterpotentials on the Recovery Cycle

CAMERON C. MCINTYRE, ANDREW G. RICHARDSON, AND WARREN M. GRILL

*Department of Biomedical Engineering, Case Western Reserve University, Cleveland, Ohio 44106-4912*

Received 30 April 2001; accepted in final form 29 October 2001

**McIntyre, Cameron C., Andrew G. Richardson, and Warren M. Grill.** Modeling the excitability of mammalian nerve fibers: influence of afterpotentials on the recovery cycle. *J Neurophysiol* 87: 995–1006, 2002; 10.1152/jn.00353.2001. Human nerve fibers exhibit a distinct pattern of threshold fluctuation following a single action potential known as the recovery cycle. We developed geometrically and electrically accurate models of mammalian motor nerve fibers to gain insight into the biophysical mechanisms that underlie the changes in axonal excitability and regulate the recovery cycle. The models developed in this study incorporated a double cable structure, with explicit representation of the nodes of Ranvier, paranodal, and internodal sections of the axon as well as a finite impedance myelin sheath. These models were able to reproduce a wide range of experimental data on the excitation properties of mammalian myelinated nerve fibers. The combination of an accurate representation of the ion channels at the node (based on experimental studies of human, cat, and rat) and matching the geometry of the paranode, internode, and myelin to measured morphology (necessitating the double cable representation) were needed to match the model behavior to the experimental data. Following an action potential, the models generated both depolarizing (DAP) and hyperpolarizing (AHP) afterpotentials. The model results support the hypothesis that both active (persistent  $\text{Na}^+$  channel activation) and passive (discharging of the internodal axolemma through the paranodal seal) mechanisms contributed to the DAP, while the AHP was generated solely through active (slow  $\text{K}^+$  channel activation) mechanisms. The recovery cycle of the fiber was dependent on the DAP and AHP, as well as the time constant of activation and inactivation of the fast  $\text{Na}^+$  conductance. We propose that experimentally documented differences in the action potential shape, strength-duration relationship, and the recovery cycle of motor and sensory nerve fibers can be attributed to kinetic differences in their nodal  $\text{Na}^+$  conductances.

## INTRODUCTION

Excitation of vertebrate nerve fibers initiates transient changes in excitability that can significantly influence subsequent impulse generation. Following a single action potential, a distinct pattern of threshold fluctuation, known as the recovery cycle, has been identified in human motor and sensory axons (Bergmans 1970; Kiernan et al. 1996; Stys and Ashby 1990). While several mechanisms have been proposed to explain these changes in excitability, the sources of the entire recovery cycle are not fully understood. The results of the present simulation study demonstrate that the recovery cycle arises from postspike afterpotentials and sodium channel activation and inactivation.

The results also demonstrate that the afterpotentials include contributions from both active and passive sources.

The recovery cycle in human motor axons is composed of absolute and relative refractory periods followed by supernormal (decreased threshold) and subnormal (increased threshold) periods (Stys and Waxman 1994). The mechanisms for the absolute and relative refractory periods in mammalian myelinated axons have been thoroughly described through mathematical models of the kinetics of the node of Ranvier, and the inactivation of fast  $\text{Na}^+$  channels is responsible for these decreases in excitability (Chiu et al. 1979). The later components of the recovery cycle have been associated with the small oscillations in axonal transmembrane potential following an action potential, referred to as the depolarizing afterpotential (DAP) and the afterhyperpolarization (AHP) (Barrett and Barrett 1982; Blight and Someya 1985; David et al. 1995). The DAP and AHP have been suggested to underlie the supernormal and subnormal periods of the recovery cycle, respectively (Bostock et al. 1998; Bowe et al. 1987). The accepted mechanism for the DAP is based on the work of Barrett and Barrett (1982), who proposed that the DAP was a result of the passive charging of the internodal axolemma during an action potential and subsequent discharging with current passing through a pathway under or through the myelin to the extracellular space. In addition to this passive mechanism, an active persistent  $\text{Na}^+$  conductance, similar to one described by Bostock and Rothwell (1997), may contribute to the DAP and corresponding supernormal period by sustaining an inward current after an action potential (Stys and Ashby 1990; Stys and Waxman 1994; Stys et al. 1993). The amplitude and time course of the DAP is limited by the continued activation of slow  $\text{K}^+$  channels, which serve to shunt current outward and reduce the charging of the internodal axolemma (David et al. 1995). The continued activation of the slow  $\text{K}^+$  channels is also the likely mechanism for the AHP and subnormal period (Baker et al. 1987; Bostock et al. 1998; David et al. 1995; Stys and Waxman 1994).

In the present study a model was developed to evaluate the proposed mechanisms for the recovery cycle of a mammalian myelinated motor axon following a single action potential. Previous modeling studies have focused only on the mechanisms responsible for the DAP (Blight 1985; Stephanova and

Address for reprint requests: W. M. Grill, Dept. of Biomedical Engineering, Case Western Reserve University, C. B. Bolton Building, Rm. 3480, Cleveland, OH 44106-4912 (E-mail: wmg@po.cwru.edu).

The costs of publication of this article were defrayed in part by the payment of page charges. The article must therefore be hereby marked "advertisement" in accordance with 18 U.S.C. Section 1734 solely to indicate this fact.

Bostock 1995). A double cable model of the axon was used that allowed separate electrical representations for the myelin and underlying internodal axolemma, as first developed by Blight (1985). Segments of nonuniform length and diameter, similar to the distributed-parameter model of Halter and Clark (1991), were used to represent the morphology of the paranode-node region in mammalian myelinated axons. The results of this study indicate that the DAP is the result of both passive (discharging of the internodal axolemma) and active (activation of nodal persistent  $\text{Na}^+$  channels) mechanisms, while the AHP is the result of activation of slow  $\text{K}^+$  channels. These afterpotentials, in combination with fast  $\text{Na}^+$  channel activation and inactivation, underlie the recovery cycle.

## METHODS

Computer-based double cable models of mammalian nerve fibers were developed with explicit representations of the nodes of Ranvier, paranodal, and internodal sections of the axon, as well as a finite impedance myelin sheath (Fig. 1). The geometry and membrane dynamics of the models were based on experimental measurements from human, cat, and rat. The models were implemented in NEURON v4.3 (Hines and Carnevale 1997) and solved using backward Euler implicit integration with a time step of 0.001–0.005 ms.

### Fiber geometry

With the exception of the double cable model of Halter and Clark (1991, 1993; Zhou and Chiu 2001; Zhou et al. 1999) (using 22

individually sized segments between successive nodes), geometric representation the internodal sections in nerve fiber models has not been strictly based on experimental morphology. Instead generically sized sections of two layers of components representing the axolemma and myelin sheath have been used (Awiszus 1990; Blight 1985; Richardson et al. 2000; Stephanova and Bostock 1995), and as a result, the fine geometrical properties of the paranode could not be accurately represented. However, the myelin attachment section of the axon has been proposed to play an important role in the DAP (Barrett and Barrett 1982), and therefore it was necessary to represent explicitly the fiber morphology. The present models used 10 segments between successive nodes with an explicit representation of the myelin attachment segment (MYSA), paranode main segment (FLUT), and internode segment (STIN) regions of the fiber (Fig. 1; Table 1). Nine models were generated, based on experimental morphology measurements (see references in Table 1), with fiber diameters ranging from 5.7 to 16.0  $\mu\text{m}$ .

### Membrane dynamics

The models used both linear and nonlinear membrane dynamics to represent the electrical behavior of the axon. The nodes consisted of the parallel combination of nonlinear fast  $\text{Na}^+$ , persistent  $\text{Na}^+$ , and slow  $\text{K}^+$  conductances, a linear leakage conductance, and the membrane capacitance (Fig. 1; Table 2). The dynamics of the nodal ion channels (equations in APPENDIX) were based on the experimental work of Scholz et al. (1993), Schwarz et al. (1995), and Reid et al. (1999). While there is evidence that slow  $\text{K}^+$  channels are present in the nodal region of the mammalian myelinated axon (Reid et al. 1999; Safronov et al. 1993; Scholz et al. 1993), and compelling arguments for the existence of persistent  $\text{Na}^+$  channels (Bostock and Rothwell 1997; Caldwell et al. 2000; Honmou et al. 1994; Smith et al. 1998), relatively little data exist describing the membrane dynamics of these channels. Therefore the parameters associated with the kinetics of these channels were selected to enable the models to reproduce a wide range of experimental data including the strength-duration relationship, current-distance relationship, conduction velocity, afterpotential shape, and excitability modulation for a range of fiber diameters. During the initial stages of model development, the membrane dynamics of Richardson et al. (2000) were used. Modifications were made to the fast  $\text{Na}^+$  channel to increase the conduction velocity and strength-duration time constant by shifting relationship between  $m_\infty$  and  $h_\infty$  and the transmembrane potential in the hyperpolarizing direction, and inactivation was slowed by increasing  $\tau_h$ . The maximum conductance density ( $g_{\text{NaP}}$ ) and time constant ( $\tau_p$ ) of the persistent  $\text{Na}^+$  channel were increased to extend the duration and amplitude of the DAP. Finally, the time constant of the slow  $\text{K}^+$  channel ( $\tau_s$ ) was increased to create an AHP that matched experimental records. The paranodal and internodal compartments consisted of two layers, each including a linear conductance in parallel with the membrane capacitance, representing the myelin sheath and underlying axolemma (Fig. 1; Table 2).

Our hypothesis is that there exists an active inward current that augments the passive discharging of the internodal axolemma responsible for the DAP (Barrett and Barrett 1982; Stys and Waxman 1994). This active inward component would need to have little or no inactivation, and a time course that would result in the depolarization lasting ~10–20 ms after the action potential spike. Previous experimental results have shown that the DAP is not mediated by calcium or chloride (Barrett and Barrett 1982), therefore a slow or persistent  $\text{Na}^+$  conductance is the most likely candidate (Honmou et al. 1994; Stys et al. 1993). The persistent  $\text{Na}^+$  conductance of our model was localized at the node of Ranvier based on experimental data demonstrating that the sodium channel subtype present in mammalian nodes of Ranvier is  $\text{Na}_v1.6$  (Caldwell et al. 2000), and orthologs of the  $\text{Na}_v1.6$  subtype are capable of generating a noninactivating current depending on the assembly of their subunits (Smith et al. 1998).

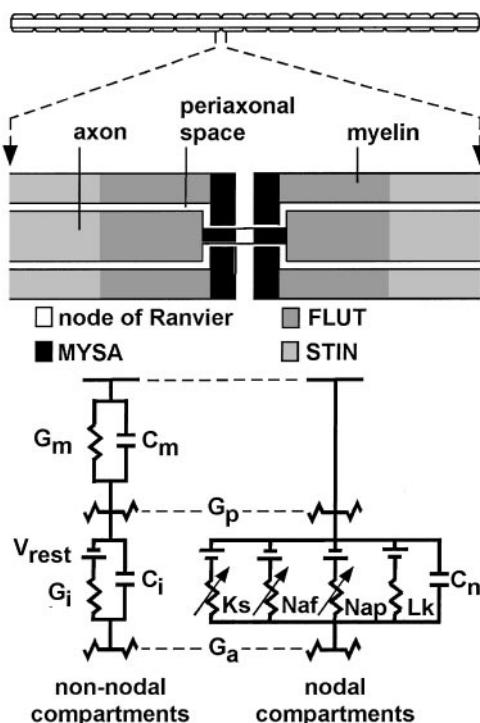


FIG. 1. Multi-compartment double cable model of a mammalian axon. The models consisted of 21 nodes of Ranvier separated by 20 internodes. Each internodal section of the model consisted of 2 paranodal myelin attachment segments (MYSA), 2 paranodal main segments (FLUT), and 6 internodal segments (STIN). The nodal membrane dynamics included fast (Naf) and persistent (Nap) sodium, slow potassium (Ks), and linear leakage (Lk) conductances in parallel with the nodal capacitance ( $C_n$ ). The internodal segments were represented by a double cable structure of linear conductances with an explicit representation of the myelin sheath ( $G_m$  in parallel with  $C_m$ ) and the internodal axolemma ( $G_i$  in parallel with  $C_i$ ).

TABLE 1. Model geometric parameters

	Fiber Diameter								
	5.7	7.3	8.7	10.0	11.5	12.8	14.0	15.0	16.0
Node-node separation <sup>a</sup>	500	750	1,000	1,150	1,250	1,350	1,400	1,450	1,500
Number of myelin lamella <sup>b</sup>	80	100	110	120	130	135	140	145	150
Node length <sup>c,d</sup>	1	1	1	1	1	1	1	1	1
Node diameter <sup>c,d</sup>	1.9	2.4	2.8	3.3	3.7	4.2	4.7	5.0	5.5
MYSA length <sup>e</sup>	3	3	3	3	3	3	3	3	3
MYSA diameter <sup>b,e</sup>	1.9	2.4	2.8	3.3	3.7	4.2	4.7	5.0	5.5
MYSA periaxonal space width <sup>e</sup>	0.002	0.002	0.002	0.002	0.002	0.002	0.002	0.002	0.002
FLUT length <sup>e</sup>	35	38	40	46	50	54	56	58	60
FLUT diameter <sup>b,e</sup>	3.4	4.6	5.8	6.9	8.1	9.2	10.4	11.5	12.7
FLUT periaxonal space width <sup>e</sup>	0.004	0.004	0.004	0.004	0.004	0.004	0.004	0.004	0.004
STIN length <sup>a</sup>	70.5	111.2	152.2	175.2	190.5	205.8	213.5	221.2	228.8
STIN diameter <sup>b</sup>	3.4	4.6	5.8	6.9	8.1	9.2	10.4	11.5	12.7
STIN periaxonal space width <sup>e</sup>	0.004	0.004	0.004	0.004	0.004	0.004	0.004	0.004	0.004

Values are expressed in  $\mu\text{m}$ . MYSA, myelin attachment section of paranode; FLUT, main section of paranode; STIN, internodal section, 6 total in 1 internode. <sup>a</sup> Nilsson and Berthold (1988). <sup>b</sup> Berthold et al. (1983). <sup>c</sup> Rydmark (1981). <sup>d</sup> Rydmark and Berthold (1983). <sup>e</sup> Berthold and Rydmark (1983).

### Simulation procedure

Simulations were conducted to measure each model's action potential and afterpotential shape, response to long duration constant current stimuli, conduction velocity, recovery cycle, threshold electrotonus, strength-duration, and current-distance properties. Both intracellular and extracellular stimuli were utilized. For intracellular stimuli, a current clamp at a node in the middle of the axon was used. For extracellular stimuli, the extracellular potentials at each compartment of the model were generated by a point source electrode placed in an infinite homogenous anisotropic medium [longitudinal resistivity =  $300 \Omega\text{-cm}$ ; transverse resistivity =  $1,200 \Omega\text{-cm}$  (Ranck and BeMent 1965)] surrounding the fiber, and equivalent sets of intracellular currents were used to simulate the influence of the extracellular electric field (Grill 1999; Richardson et al. 2000; Warman et al. 1992).

TABLE 2. Model electrical parameters

Nodal capacitance <sup>a</sup> ( $c_n$ )	$2 \mu\text{F}/\text{cm}^2$
Internodal capacitance <sup>b</sup> ( $c_i$ )	$2 \mu\text{F}/\text{cm}^2$
Myelin capacitance <sup>c,d,e</sup> ( $c_m$ )	$0.1 \mu\text{F}/\text{cm}^2$
Axoplasmic resistivity ( $\rho_a$ )	$70 \Omega\text{ cm}$
Periaxonal resistivity ( $\rho_p$ )	$70 \Omega\text{ cm}$
Myelin conductance <sup>c,d,e</sup> ( $g_m$ )	$0.001 \text{ S}/\text{cm}^2$
MYSA conductance ( $g_a$ )	$0.001 \text{ S}/\text{cm}^2$
FLUT conductance ( $g_f$ )	$0.0001 \text{ S}/\text{cm}^2$
STIN conductance ( $g_i$ )	$0.0001 \text{ S}/\text{cm}^2$
Maximum fast $\text{Na}^+$ conductance <sup>f,g,h</sup> ( $g_{\text{Na}f}$ )	$3.0 \text{ S}/\text{cm}^2$
Maximum slow $\text{K}^+$ conductance <sup>f,h,i</sup> ( $g_{\text{K}s}$ )	$0.08 \text{ S}/\text{cm}^2$
Maximum persistent $\text{Na}^+$ conductance <sup>j</sup> ( $g_{\text{Na}p}$ )	$0.01 \text{ S}/\text{cm}^2$
Nodal leakage conductance ( $g_{\text{Lk}}$ )	$0.007 \text{ S}/\text{cm}^2$
$\text{Na}^+$ Nernst potential <sup>k</sup> ( $E_{\text{Na}}$ )	$50.0 \text{ mV}$
$\text{K}^+$ Nernst potential <sup>k</sup> ( $E_{\text{K}}$ )	$-90.0 \text{ mV}$
Leakage reversal potential ( $E_{\text{Lk}}$ )	$-90.0 \text{ mV}$
Rest potential <sup>k</sup> ( $V_{\text{rest}}$ )	$-80.0 \text{ mV}$

<sup>a</sup> Frankenhaeuser and Huxley (1964). <sup>b</sup> Bostock and Sears (1978). <sup>c</sup> Per lamella membrane (2 membranes per lamella). <sup>d</sup> Huxley and Stampfli (1949). <sup>e</sup> Tasaki (1955). <sup>f</sup> Scholz et al. (1993). <sup>g</sup> Waxman and Ritchie (1993). <sup>h</sup> Schwarz et al. (1995). <sup>i</sup> Saffronov et al. (1993). <sup>j</sup> Bostock and Rothwell (1997). <sup>k</sup> Stys et al. (1997).

### RESULTS

Computer models of mammalian motor nerve fibers were developed to examine the biophysical mechanisms underlying changes in axonal excitability following an action potential. The combination of an accurate representation of both the fiber geometry and the nodal membrane dynamics allowed the models to reproduce multiple sets of independent experimental data. The depolarizing (DAP) and hyperpolarizing (AHP) afterpotentials generated following an action potential were directly related to the recovery cycle of the fiber, and the model

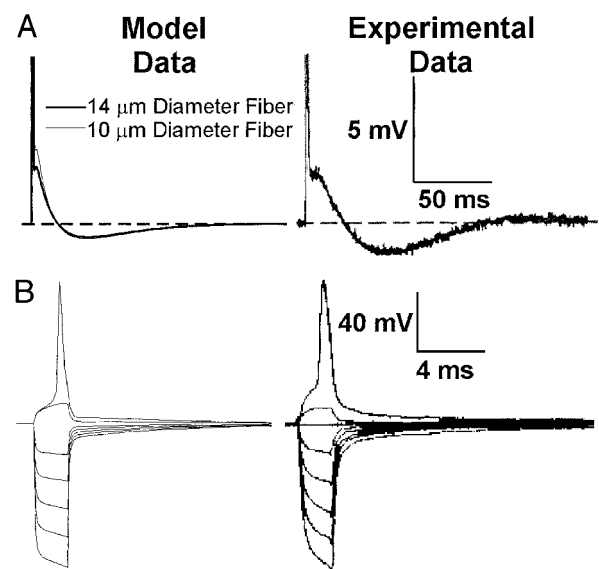


FIG. 2. Axonal action potential and afterpotential shape. A: following an action potential (spike amplitude truncated), the models generated depolarizing and hyperpolarizing afterpotentials that matched well with intra-axonal recordings from rat (David et al. 1995) (spike amplitudes truncated). B: the models responded to 2-ms hyperpolarizing stimuli with hyperpolarizing afterpotentials that matched well with experimental recordings from cat (Blight and Someya 1985).



results support the hypothesis that both active and passive mechanisms contribute to the DAP, while the AHP is generated solely through active mechanisms. The recovery cycle was also dependent on the time constant of activation and inactivation of the fast  $\text{Na}^+$  channel.

### Action potential and afterpotential shape

Model responses to short-duration (100  $\mu\text{s}$ ) suprathreshold stimuli exhibited a DAP of  $\sim 15$  ms followed by an AHP of  $\sim 80$  ms (durations were dependent on fiber diameter) that closely matched intracellular recordings from myelinated rat motor nerve fibers (David et al. 1995) (Fig. 2A). The models also exhibited a diameter-dependent DAP amplitude (increasing DAP amplitude with decreasing fiber diameter), regulated by changes in the fiber geometry, which has been suggested by experimental work but never explicitly recorded (Barrett and Barrett 1982; David et al. 1995). The model responses to hyperpolarizing (2 ms) stimuli showed a hyperpolarizing afterpotential, generated by the passive discharging of the internodal axolemma, that also matched experimental results (Blight and Someya 1985) (Fig. 2B).

### Passive and active contributions to the afterpotentials

Afterpotentials generated by the axon models were dependent on both active and passive mechanisms (Figure 3). The work of Barrett and Barrett (1982) proposed that the DAP was the result of the passive charging of the internodal axolemma during an action potential and subsequent discharging with current passing through a pathway under or through the myelin to the extracellular space. We used a totally passive version of our model, with all conductances fixed at rest values, to study the parameters effecting this contribution to the DAP. A pseudo action potential was generated by injecting a 500- $\mu\text{s}$  current pulse resulting in the same area under the spike as a normal action potential (Fig. 3, A2–A4). The amplitude of the DAP in the passive model was reduced, its duration was increased compared with the full model, and the AHP was absent. The presence of the paranodal seal resistance, magnitude of the axolemma conductance in the paranode myelin attachment segment (MYSA), and the length of the paranode main segment (FLUT) influenced the passive DAP. Replacing the finite paranodal seal resistance with an infinite resistance completely abolished the passive DAP (Fig. 3A3). Increasing the axolemma conductance ( $g_i$ ) in the MYSA resulted in a

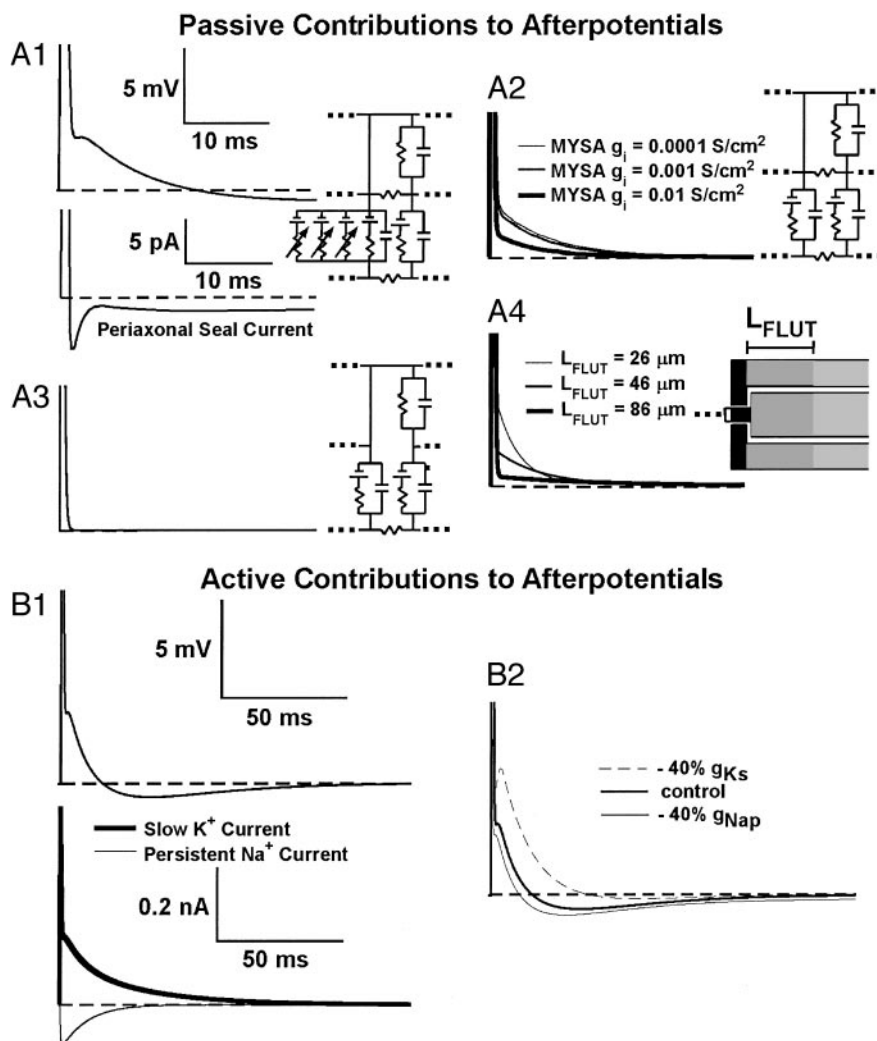


FIG. 3. Origin of the afterpotentials. A1: the 10.0- $\mu\text{m}$  fiber diameter full model showed depolarizing (DAP) and hyperpolarizing (AHP) afterpotentials. The current through the periaxonal seal resistance produced the passive component of the DAP (spike amplitudes truncated). A2: removal of the nonlinear membrane dynamics of the node and generation of a pseudo action potential (injection of a 500- $\mu\text{s}$  current pulse resulting in the same area under the spike as a normal action potential) illustrates the passive contribution to the DAP and how it is effected by alterations in the paranodal axolemma conductance. A3: setting the paranodal seal resistance to  $\infty$  resulted in a dramatic decrease in the passive DAP. A4: alterations in the length of the paranode main segment changed the time course and amplitude of the passive component of the DAP. B1: the 10.0- $\mu\text{m}$  fiber diameter full model showing the DAP and AHP and corresponding slow  $\text{K}^+$  and persistent  $\text{Na}^+$  currents. B2: independent alteration (40% reduction) in the maximum conductance of the slow  $\text{K}^+$  or persistent  $\text{Na}^+$  currents altered both the time course and amplitude of the DAP and AHP shape compared with the default model.

decrease in the DAP amplitude (Fig. 3A2). Further, increases in the overall length of the paranode increased the time constant of decay and decreased the amplitude of the passive component of the DAP (Fig. 3A4). Therefore an accurate representation of the paranodal region of the model axon was important in generating the DAP.

The passive discharge of the internodal axolemma contributed to the DAP, but alone was insufficient to reproduce experimentally measured afterpotentials. In addition to the passive mechanism, an active persistent  $\text{Na}^+$  conductance contributed to the DAP by sustaining an inward current after an action potential (Fig. 3B1) and also resulted in a slight increase in DAP amplitude following the spike (Fig. 3A1), which has also been recorded experimentally (Fig. 2A, David et al. 1995). The amplitude and time course of the DAP was limited by the activation of the nodal slow  $\text{K}^+$  channels, which shunted current outward and reduced the charging of the internodal axolemma. The continued activation of slow  $\text{K}^+$  channels was also the mechanism responsible for the AHP (Fig. 3B1). Approximately 25 ms after an action potential, the persistent  $\text{Na}^+$  current had returned to baseline while an outward current from the slow  $\text{K}^+$  channel remained, terminating the DAP and generating the AHP. Alterations in the density of the slow  $\text{K}^+$  or persistent  $\text{Na}^+$  channels effected the duration and amplitude of both the DAP and AHP (Fig. 3B2). A 40% decrease in the density of the slow  $\text{K}^+$  channel resulted in an increase in the duration and amplitude of the DAP combined with a decrease in the duration and amplitude of the AHP, and a 40% reduction in the density of the persistent  $\text{Na}^+$  channel resulted in a decrease in the duration and amplitude of the DAP combined with an increase in the duration and amplitude of the AHP. Thus in addition to the passive discharge of the internodal axolemma, active ionic currents contributed to the afterpotentials.

### Recovery cycle

The models exhibited a supernormal period (period of increased excitability) after a subthreshold conditioning pulse (Fig. 4A), which has been observed experimentally (Bowe et al. 1987). The subthreshold supernormal period was generated primarily by a passive DAP that followed the subthreshold stimulus. However, the increase in excitability was also augmented by the slight activation of the persistent  $\text{Na}^+$  conductance and slight opening of the activation gate of the fast  $\text{Na}^+$  conductance.

The models generated both supernormal and subnormal periods (the recovery cycle) after suprathreshold conditioning pulses that closely matched experimental results (Kiernan et al. 2000) (Fig. 4B). The shape of the recovery cycle of the fibers was linked to the depolarizing and hyperpolarizing afterpotentials. The shape of the recovery cycle was also dependent on the diameter of the fiber with smaller diameter fibers exhibiting greater changes in threshold. The fiber diameter dependence of the recovery cycle was related to the fiber diameter dependence of the shape of the afterpotentials (Fig. 2A). Smaller diameter fibers generated a greater passive DAP, resulting in a greater supernormal period. The increase in the DAP amplitude and duration enhanced and prolonged the activation of the slow  $\text{K}^+$  conductance, resulting in a greater subnormal period.

The shape of the recovery cycle was also dependent on the

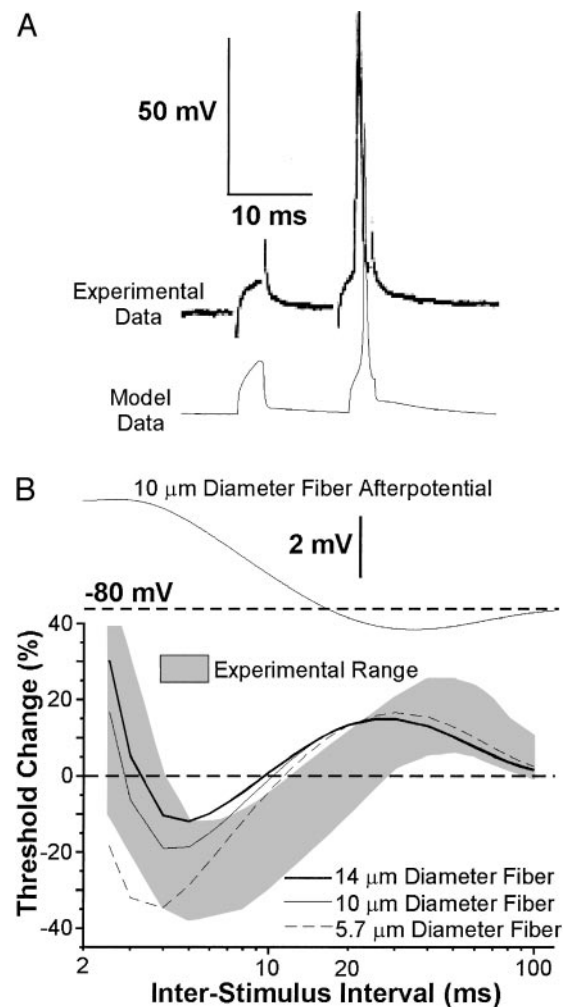


FIG. 4. Relation of afterpotentials to axonal excitability and the recovery cycle. A: when 2 subthreshold 3-ms stimuli, separated by 13 ms, were applied to the model, the 2nd stimuli resulted in a suprathreshold response, which matched experimental records from rat (Bowe et al. 1987). B: a suprathreshold 1-ms conditioning stimulus was followed (after given interval) by a 1-ms test stimulus, and threshold for activation was determined. The models exhibited a period of decreased excitability (relative refractory), followed by a period of increased excitability (supernormal), followed by a period of decreased excitability (subnormal), which corresponded to experimental results in human (Kiernan et al. 2000). The 10- $\mu\text{m}$ -diam fiber afterpotential from a suprathreshold stimulus is plotted on the same time scale as the recovery cycle to illustrate the correspondence between the supernormal and subnormal periods and the depolarizing afterpotential and hyperpolarizing afterpotential, respectively.

activation and inactivation of the fast  $\text{Na}^+$  conductance. The time constants of the activation gate ( $\tau_m$ ; Fig. 5A) and the inactivation gate ( $\tau_h$ ; Fig. 5B) were independently altered to examine their role in the shape of the recovery cycle. Slowing  $\tau_m$  made the membrane less excitable, and, as a result, the amplitude and duration of the supernormal period was decreased, while the subnormal period was increased. Speeding up  $\tau_m$  made the membrane more excitable and in turn resulted in an increase in the supernormal period and a decrease in the subnormal period.

When  $\tau_h$  was altered, the effects on the recovery cycle were opposite to those caused by changing  $\tau_m$  (Fig. 5B). Speeding up  $\tau_h$  resulted in a decrease in the supernormal period and an increase in the subnormal period, and slowing down  $\tau_h$  resulted in an increase in the supernormal period and a decrease in the

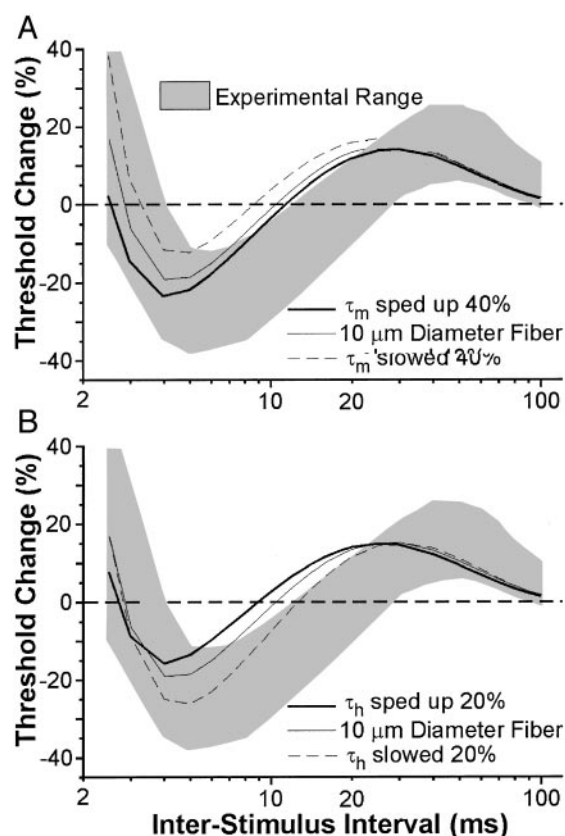


FIG. 5. Influence of  $\text{Na}^+$  channel activation and inactivation on the recovery cycle. *A*: the time constant of the activation gate of the nodal fast  $\text{Na}^+$  channel ( $\tau_m$ ) was increased or decreased by 40%, and the recovery cycle was compared with the default 10- $\mu\text{m}$ -diam fiber model. *B*: the time constant of the inactivation gate of the nodal fast  $\text{Na}^+$  channel ( $\tau_h$ ) was increased or decreased by 20%, and recovery cycle was compared with the default 10- $\mu\text{m}$ -diam fiber model.

subnormal period. The recovery cycle was more sensitive to changes in  $\tau_h$  than changes in  $\tau_m$ , but alterations in the  $h$  gate had an indirect influence on the recovery cycle of the fiber. In the case of a slowed  $\tau_h$ , the action potential resulting from the conditioning pulse was broader due to the slow closing of the inactivation gate. This created a greater charging of the inter-nodal axolemma and continued activation of the persistent  $\text{Na}^+$  conductance resulting in a DAP with enhanced amplitude and duration. Because of the larger DAP, 4–5 ms after the conditioning stimulus, the  $m$  gate was less closed, and the  $h$  gate had returned to an open enough state to allow for a subsequent action potential. As a result the fiber was more excitable, and the supernormal period lasted longer.

#### Impulse-dependent AHP

The models generated a late AHP after a train of high-frequency (200 Hz) suprathreshold stimuli (200  $\mu\text{s}$ ). The amplitude and duration of the AHP was dependent on the duration of the stimulus train (Fig. 6) (Baker et al. 1987; Bergmans 1970; Lin et al. 2000). The models exhibited a period of subexcitability (H1) associated with the late AHP that was regulated by an increase in the slow potassium conductance during subsequent impulses and lasted for  $\sim 100$  ms after the cessation of the stimulus train. The magnitude and duration of H1 was dependent on the fiber diameter with smaller fibers

having a more pronounced H1 than larger fibers. With a train of 10 conditioning stimuli, the 10- $\mu\text{m}$ -diam fiber exhibited a peak in subnormality (24% increased threshold relative to unconditioned stimuli) at a conditioning-test interval of 25 ms, while the 14- $\mu\text{m}$ -diam fiber exhibited a 20% peak increase in threshold at a conditioning-test interval of 25 ms. Nonetheless, both match well with the experimental results of Bergmans (1970) and Lin et al. (2000).

#### Threshold electrotonus and spike frequency accommodation

Prolonged subthreshold currents are used to alter the nodal and internodal transmembrane potential as a method to gain insight into the ion channels of the axon (Baker et al. 1987). The pattern of alteration in threshold induced by a subthreshold current pulse ( $\sim 100$  ms in duration) is termed threshold electrotonus (Bostock et al. 1991; Yang et al. 2000). The axon models captured the general shape of experimentally measured threshold electrotonus from rat (Fig. 7A) but were unable to accurately match the magnitude of the transient changes in threshold seen in human subjects (see DISCUSSION).

Model responses to long-duration suprathreshold constant current depolarizing stimuli exhibited spike frequency accommodation (Fig. 7B) that corresponded to experimental results (Baker et al. 1987; Schwarz et al. 1995). This accommodation was present at all stimulus levels; near rheobase one spike was generated, and, as the stimulation intensity was increased, two to five spikes occurred before complete accommodation. Accommodation was the result of continued activation of the slow  $\text{K}^+$  current that effectively shunted the inward currents responsible for the generation of subsequent action potentials (Baker et al. 1987; Schwarz et al. 1995), while the depolarization resulting from the stimulus maintained the fast  $\text{Na}^+$  channels in a relatively inactivated state. Continued activation of the slow  $\text{K}^+$  current also resulted in a poststimulus hyperpolarization of 1–3 mV, depending on the duration and amplitude of the stimulus train.

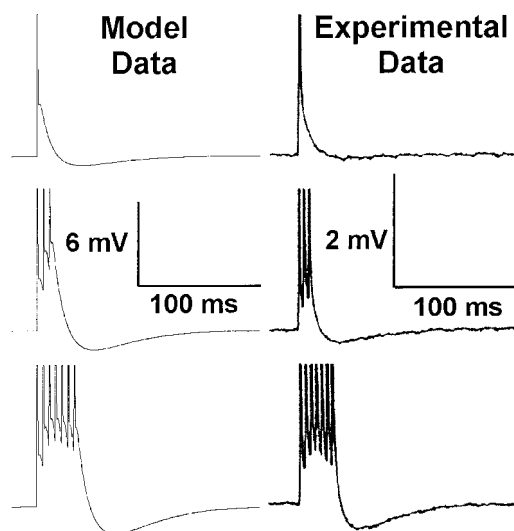


FIG. 6. Impulse-dependent afterhyperpolarization (AHP). The models exhibited an increase in the AHP amplitude and duration with an increase in the number of high-frequency (200 Hz) suprathreshold 100- $\mu\text{s}$  stimuli applied, which matched well with experimental recordings from rat (Baker et al. 1987) (spike amplitudes truncated).



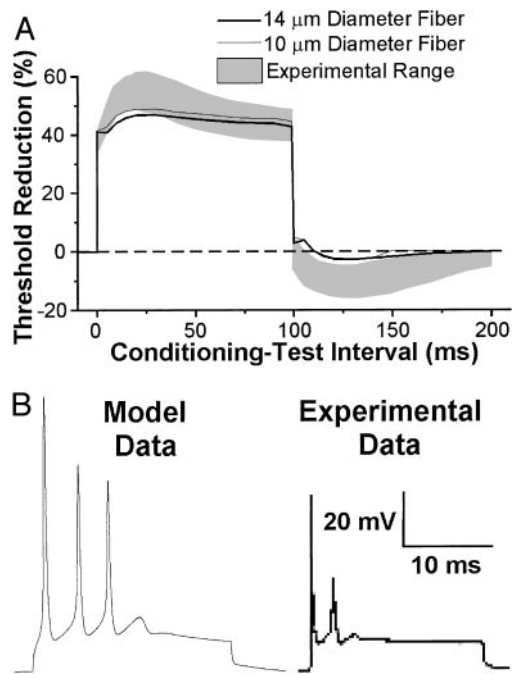


FIG. 7. Threshold electrotonus and spike frequency accommodation. *A*: a conditioning stimulus of 40% threshold was applied for 100 ms, and the threshold for action potential initiation with a 1-ms test pulse was determined during and after the conditioning pulse. The models were able to reproduce the changes in threshold measured in rat (Yang et al. 2000). *B*: long-duration suprathreshold constant current stimuli resulted in spike frequency accommodation after 1–5 spikes, dependent on the stimulus amplitude, corresponding to experimental records from rat (Baker et al. 1987).

#### Conduction velocity, strength-duration, and current-distance relationships

Action potential conduction velocity (CV) was dependent on the fiber diameter (D) (Fig. 8*A*). The model CV closely matched experimental measurements from cat afferent nerve fibers for fiber diameters ranging from 5.7 to 16  $\mu\text{m}$  (Boyd and Kalu 1979). The relationship between D and CV is dependent on a host of factors including myelin thickness and internodal length (Waxman 1980), and it has been suggested that differences in the type and density of the nodal sodium channels of different sized fibers can also play a role (Jack 1975). However, the CV relationship of the axon models arose solely through geometrical differences between the different diameter models (see Table 1), indicating that differences in the nodal ionic channels are not required to explain diameter-dependent CV.

The strength-duration relationship (threshold stimulus current as a function of stimulus pulse duration) was generated with extracellular electrodes at a range of different positions (Fig. 8*B*). The model results matched well with results from human subjects (Panizza et al. 1994, 1998). The results also suggested that smaller diameter fibers have longer chronaxies than larger diameter fibers. However, chronaxie times measured with extracellular stimulation were dependent on the electrode position relative to the neural structure, and the shortest chronaxie times were found with the electrode nearest to a node of the axon.

The current-distance relationship (threshold stimulus current as a function of electrode-to-axon distance) was generated with an extracellular electrode and a random distribution of 50

10- $\mu\text{m}$  and 50 14- $\mu\text{m}$  fibers. The perpendicular distances between the fibers and the electrode were uniformly distributed over a range of 100–1,000  $\mu\text{m}$ , and the lateral positions of the central node of the fibers were uniformly distributed over a range of zero to one-half of one internodal length (Fig. 8*C*). The model results matched well with results from microstimulation of fibers in the cat spinal cord (BeMent and Ranck 1969; Roberts and Smith 1973). The results also suggest that larger diameter fibers have smaller  $k$  values, or a lower slope of the current-distance relationship, than smaller diameter fibers.

#### Role of juxtaparanodal $\text{K}^+$ channels in axonal excitability

Recent experimental studies have demonstrated segregation of fast  $\text{K}^+$  channels at the juxtaparanodal regions of the axolemma (Vabnick et al. 1999). Therefore we developed a modified version of our 10- $\mu\text{m}$ -diam fiber that incorporated a fast  $\text{K}^+$  conductance, based on the experimental work of Schwarz et al. (1995) (equations in APPENDIX), located in the FLUT region of the fiber (Vabnick et al. 1999). The appropriate conductance density of the juxtaparanodal fast potassium channel is unclear. The work of Roper and Schwarz (1989) and Safronov et al. (1993) suggest the channel density for fast potassium channels in the juxtaparanode is  $\sim 12/\mu\text{m}^2$  and the single channel conductance is  $\sim 17$  pS, resulting in a maximum conductance density ( $g_{\text{Kf}}$ ) of  $\sim 0.02$  S/ $\text{cm}^2$ . We examined a range of different model parameter sets with a juxtaparanodal  $g_{\text{Kf}}$  that ranged from 0.01 to 0.04 S/ $\text{cm}^2$ . The inclusion of fast potassium conductance in the FLUT regions of the model resulted in a decrease in the amplitude and duration of the DAP and a corresponding decrease in the supernormal period (Fig. 9*A*). The inclusion of paranodal potassium channels also resulted in alterations of threshold electrotonus including a smaller decrease in the threshold at the beginning of the conditioning pulse and a larger increase in threshold at the termination of the conditioning pulse (Fig. 9*B*).

#### DISCUSSION

We used computational models of mammalian motor nerve fibers to explore the biophysical mechanisms underlying changes in excitability following an action potential. The model results support a hypothesis of both active (persistent  $\text{Na}^+$  channel activation) and passive (discharging of the internodal axolemma through the paranodal seal) contributions to the DAP, while the AHP was generated solely through active (slow  $\text{K}^+$  channel activation) mechanisms. The recovery cycle of the fiber following an action potential arose from the depolarizing (DAP) and hyperpolarizing (AHP) afterpotentials and the kinetics of the fast  $\text{Na}^+$  conductance. The results from this study show that accurate representations of both the fiber geometry (especially the node-paranode region) and the nodal membrane dynamics were necessary to reproduce a wide range of independent experimental data.

#### Model limitations

The models developed in this study had three primary limitations. First, the ion channel types, densities, and membrane dynamics of the mammalian node of Ranvier are not completely characterized (Baker et al. 1987; Chiu et al. 1979; Reid et al. 1999; Safronov et al. 1993; Scholz et al. 1993; Schwarz

et al. 1995). Therefore our model included a simplified representation, based on available experimental data, of some of the ion channels present in the node. Although based on experimental current- and voltage-clamp recordings, the parameters describing the nodal ion channels were modified to enable the

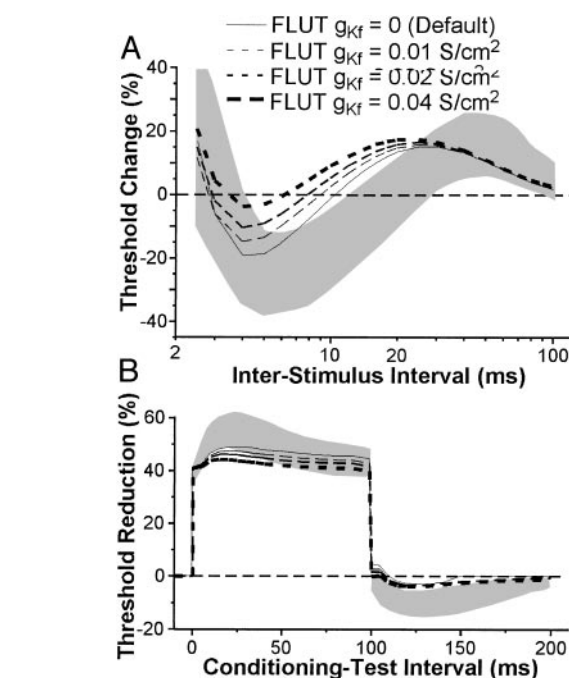
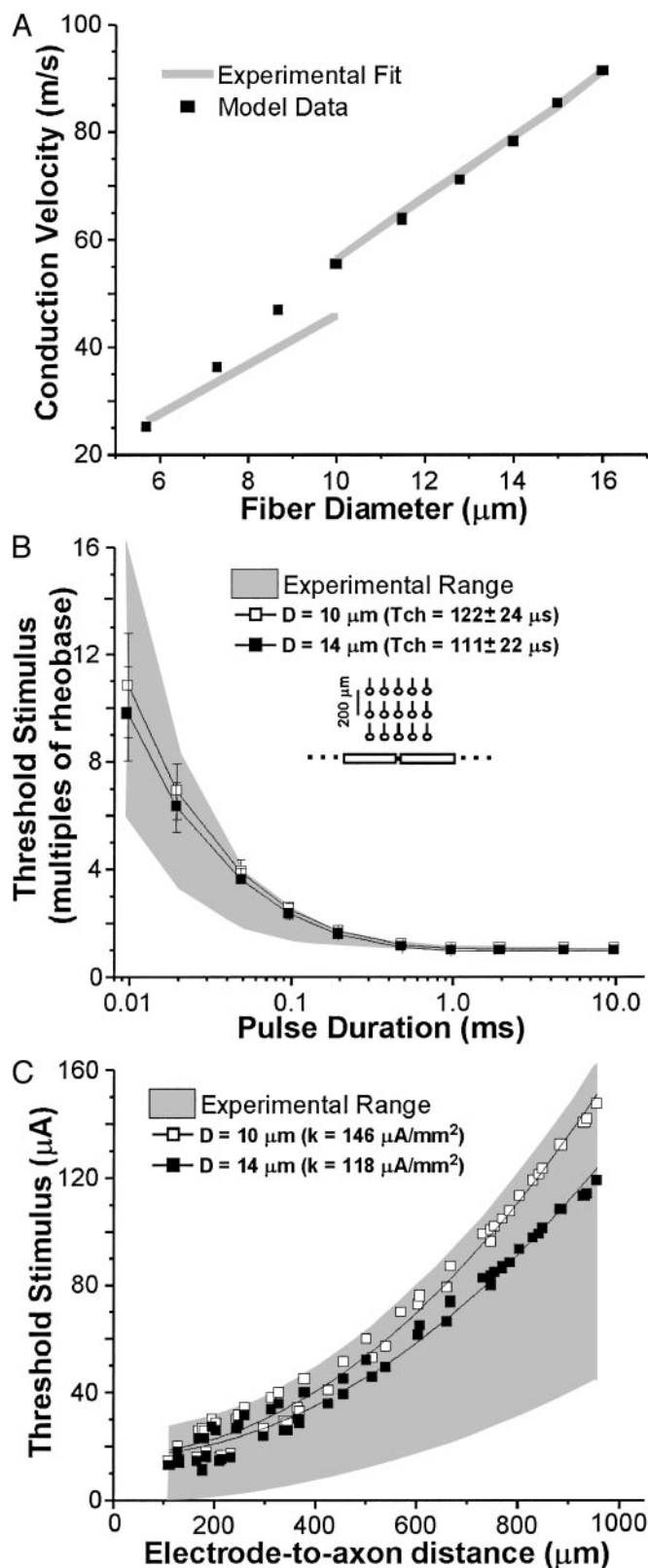


FIG. 9. Role of juxtaparanodal fast  $\text{K}^+$  channels on the recovery cycle and threshold electrotonus. **A**: recovery cycle of the 10- $\mu\text{m}$ -diam model over a range of conductance densities for the juxtaparanodal fast  $\text{K}^+$  channel (see METHODS) compared with the recovery cycle measured in humans (Kiernan et al. 2000). **B**: threshold electrotonus of the 10- $\mu\text{m}$ -diam model over a range of conductance densities for the juxtaparanodal fast  $\text{K}^+$  channel compared with changes in threshold measured in rat (Yang et al. 2000).

reproduction of several different experimentally documented excitation characteristics. The implication of such an approach is that the ion channels used in the model may actually represent the condensation of several different types of channels into single equivalent channels. For example, only a single type of slow potassium channel was included in our default model. However, five different types of fast, slow, and intermediate potassium channels have been recorded in human nerve fibers (Reid et al. 1999). Even with this potential limitation, the model results and conclusions are well grounded in complementary experimental work. As a result, we feel the simplified representation of the different ion channels is justified, and it allowed for identification and examination of the general biophysical mechanisms regulating axonal excitability following an action potential.

The second limitation of the models was the representation of the axon membrane under the myelin as a linear conduc-

FIG. 8. Conduction velocity (CV), strength-duration (S-D), and current-distance (I-X) relationships. **A**: the model CV matched well with experimental fits to fiber diameter ( $D$ ) dependent changes in CV recorded in cat [ $CV = 4.60 \cdot D$  (smaller diameter fibers);  $CV = 5.66 \cdot D$  (larger diameter fibers)] (Boyd and Kalu 1979). **B**: the model S-D relationships matched with experimental ranges [chronaxie ( $T_{ch}$ ) = 50–150  $\mu\text{s}$ ] determined with extracellular activation of human motor axons (Panizza et al. 1994, 1998). The average and SD of threshold ( $I_{th}$ ) relative to rheobase ( $I_{rh}$ ) are plotted for the models from the 15 different electrode positions shown in the inset. The chronaxie was estimated from a least-squares log-log fit to  $I_{th} = I_{rh} \cdot [1 + (T_{ch}/PD)]$ , where PD was the pulse duration (McIntyre and Grill 1998). **C**: the model I-X relationships for 100- $\mu\text{s}$  stimuli (least-squares fit to  $I_{th} = I_o + k \cdot r^2$ , where  $I_{th}$  was the estimated threshold current,  $I_o$  was the offset,  $k$  was the slope, and  $r$  was the electrode-to-axon distance) matched well with experimental ranges ( $I_o = 0$ –25  $\mu\text{A}$ ;  $k = 50$ –150  $\mu\text{A}/\text{mm}^2$ ) determined in the cat (BeMent and Ranck 1969; Roberts and Smith 1973).



tance in parallel with the membrane capacitance. A wide range of different ionic conductances are present in the internodal sections of the axon, including several different types of potassium channels, sodium channels, and sodium and potassium pumps (Baker et al. 1987; Bostock et al. 1991; Waxman and Ritchie 1993). These channels and pumps have been proposed to play a role in several different excitation properties of the axon and in maintaining the rest potential. Internodal channels and pumps were not included in our models for two reasons: the resultant increase in computational complexity and the lack of explicit characterizations of their dynamic properties (i.e., parameter uncertainty). Our goal was to generate the simplest models possible using physiological plausible mechanisms to reproduce many different sets of independent experimental data, and use these models to explain changes in post-action potential excitability. While the addition of internodal channels and pumps would make the model more complete, the added computational complexity, parameter uncertainty, and difficulty in identifying the major contributions to a specific behavior, make the exclusion of internodal channels and pumps valid for the purposes of this study. However, the major weakness of this approach for the examination of afterpotentials and activity-dependent excitability is the neglect of juxtaparanodal fast  $K^+$  channels (Vabnick et al. 1999). Therefore we performed a sensitivity analysis of the role of the conductance density of a juxtaparanodal fast  $K^+$  conductance on the recovery cycle and threshold electrotonus (Fig. 9). The results show that, when realistic densities of fast  $K^+$  channels are included ( $\sim 0.02$  S/cm<sup>2</sup>), there are limited effects on the afterpotentials and the excitation properties of the model.

As a result of our simplified representation of the internodal membrane dynamics, the models exhibited slight discrepancies with the experimental records of threshold electrotonus and spike frequency accommodation. Specifically the models were unable to capture the magnitude of the transient changes in threshold electrotonus, and firing did not accommodate to long-duration suprathreshold stimuli as rapidly as experimental records (Fig. 7). Both of these behaviors have been linked to activation of internodal ion channels and ionic pumps (Baker et al. 1987; Bostock et al. 1991). Thus the model results reinforce the importance internodal and paranodal channels and pumps in activity-dependent modulation of excitability, and the model complexity is not sufficient to draw conclusions on the complete mechanisms of threshold electrotonus or spike frequency accommodation. It should also be noted that our model threshold electrotonus was compared with experimental results from rat, but a substantial difference exists in the threshold electrotonus of humans and rats where humans exhibit larger transient changes in threshold both during and after the conditioning stimulus (Yang et al. 2000), suggesting a difference in the ion channel distributions and/or densities in the two species.

The final limitation of our models was the lack of a representation of potassium accumulation in the extracellular space. When axons fire long trains of impulses, potassium concentration in the extracellular space can increase, especially in the periaxonal space (David et al. 1993; Zhou and Chiu 2001). This increase in extracellular potassium can increase the excitability of the axon, lead to ectopic discharge (Kapoor et al. 1993), and may play an important role when the axon fires at high frequencies for extended periods of time (Bostock and Bergmans 1994). However, for single spikes or short trains of

spikes, as used in this study, potassium accumulation should not substantially impact fiber excitability. Even with these limitations, the models were able to reproduce a wide range of experimentally documented excitation patterns, and thus represent powerful tools to explore mechanisms responsible for activity-dependent changes in axonal excitability.

### *Origin of afterpotentials*

Mammalian myelinated axons exhibit both depolarizing and hyperpolarizing afterpotentials (David et al. 1995) that can result in substantial changes in axonal excitability (Bergmans 1970; Kiernan et al. 1996) (Fig. 4). The results of this study indicate that there are two important contributions to these afterpotentials. The first contribution is the passive discharging of the internodal axolemma through the paranodal seal (Fig. 3) (Barrett and Barrett 1982). Reproduction of this component of the DAP required models that represented accurately the fiber morphology, particularly in the node-paranode region (Table 2). In earlier versions of our axon models (Richardson et al. 2000), it was not possible to generate a passive DAP of appropriate amplitude without explicit representation of the geometry of the node-paranode region. The use of separate compartments for the paranode myelin attachment segment (MYSA) and paranode main compartment (FLUT) and inclusion of a realistic paranodal seal resistance were very important to the generation of a passive DAP (Fig. 3A). The length of the paranodal region of the fibers used in the models was based on the experimentally determined percentage of the total internodal length ( $\sim 5\%$ ) (Berthold and Rydmark 1983); however, alterations in the length of the paranode effected the DAP amplitude and time constant of decay.

The second contribution to the afterpotentials arose from the nonlinear membrane dynamics of the node. The activation of persistent  $Na^+$  channels augmented the passive mechanism and increased the amplitude of the DAP. Previous results suggested that the DAP was a result of only the passive mechanism; however, in the generation of that hypothesis, the AHP was not considered (Barrett and Barrett 1982). Our results indicate that when using voltage-gated slow  $K^+$  channels to produce the AHP (Baker et al. 1987; David et al. 1995), the only way to maintain an accurate DAP amplitude and realistic supernormal period is to have an active component to augment the passive DAP (Figs. 3 and 4). A persistent  $Na^+$  current is responsible for DAPs in CA1 pyramidal neurons (Azouz et al. 1996), and subfornical organ neurons (Washburn et al. 2000), but experimental verification that persistent  $Na^+$  currents augment the DAP in myelinated axons does not presently exist. Thus the finding that a persistent  $Na^+$  current is necessary to produce a realistic DAP amplitude and supernormal period in mammalian myelinated axons is only a model prediction. Experimental results on myelinated axons have shown that the amplitude and time course of the DAP is limited by the continued activation of slow  $K^+$  channels, which serve to shunt outward current and reduce the charging of the internodal axolemma (David et al. 1995). The model results suggest that the continued activation of the slow  $K^+$  channels is also the mechanism for the AHP (Fig. 3). Therefore the model results support a hypothesis of both active and passive contributions to the generation of afterpotentials.

### *Pharmacological evidence for the role of nonlinear ion channels in afterpotentials*

Experimental investigations have shown that TTX (which blocks  $\text{Na}^+$  channels, including persistent  $\text{Na}^+$  channels), 4-aminopyridine (4-AP; which blocks fast  $\text{K}^+$  channels), and tetraethylammonium (TEA; which blocks most  $\text{K}^+$  channels, including the kinetically slower 4-AP-insensitive channels) affect the amplitude and duration of the DAP and AHP (Barrett and Barrett 1982; Barrett et al. 1988; Bowe et al. 1987; Eng et al. 1988). Changes in afterpotentials resulting from alterations in the conductance densities of the ionic currents in the model were consistent with these pharmacological studies. Decreasing the nodal  $g_{\text{Nap}}$  (analogous to TTX application) resulted in a decrease in the duration and amplitude of the DAP (Fig. 3B2), and experimental application of TTX resulted in a decrease in the action potential (AP) amplitude and duration, and a decrease in the DAP amplitude and duration (Barrett and Barrett 1982). Decreasing the nodal  $g_{\text{Ks}}$  (analogous to TEA application) increased the amplitude and duration of the DAP and decreased the amplitude of the AHP (Fig. 3B2). Application of TEA experimentally resulted in only slight AP broadening; however, there were substantial increases in the DAP amplitude and duration and decreases in the AHP amplitude and duration (Barrett et al. 1988; Bowe et al. 1987; Eng et al. 1988). Decreasing the paranodal  $g_{\text{Kf}}$  (analogous to 4-AP application) increased the amplitude and duration of the DAP (reflected in the increased amplitude and duration of the supernormal period in Fig. 9A). Experimentally, application of 4-AP resulted in broadening of the AP and a slight increase in the amplitude and duration of the DAP (Bowe et al. 1987; Eng et al. 1988). Thus the changes in model afterpotentials resulting from changes in conductance densities were consistent with experimental measurements of afterpotentials in the presence of channel blockers and further illustrate the role of active ionic currents in the generation of afterpotentials and the recovery cycle.

### *Relation of the afterpotentials and the recovery cycle*

Our model data agreed well with the experimentally measured recovery cycle (Fig. 3B) (Kiernan et al. 1996, 2000; Lin et al. 2000). The results of this study show that the recovery cycle of the fiber is regulated by the afterpotentials generated following an action potential as well as the kinetics of the fast  $\text{Na}^+$  conductance. However, one unanswered question related to the mechanisms of the recovery cycle is why a greater super- and subnormality exists in motor axons than sensory axons (Kiernan et al. 1996). The difference between the strength-duration time constant ( $\tau_{\text{SD}}$ ) of motor and sensory fibers has been well documented (Bostock and Rothwell 1997; Mogyoros et al. 1996; Panizza et al. 1994). It has been suggested that there are differences in the ion channels of these different fiber types, specifically a greater density of persistent  $\text{Na}^+$  channels in sensory than motor fibers that act to depolarize the sensory fibers and increase  $\tau_{\text{SD}}$  (Bostock and Rothwell 1997; Burke et al. 1998; Honmou et al. 1994). The similarity in the shapes of the recovery cycles motor and sensory fibers suggests that similar mechanisms are responsible for the recovery cycle in both fiber types. However, the results from this study, indicating that persistent  $\text{Na}^+$  channels play an important role in the

DAP and subsequent supernormal period, suggest that an increased density of persistent  $\text{Na}^+$  channels would result in a greater, rather than smaller, supernormal period in sensory fibers compared with motor fibers (Fig. 3B).

How can these conflicting roles for the persistent  $\text{Na}^+$  channel be resolved? Possibly the differences in  $\tau_{\text{SD}}$  are regulated more by differences in the “fast”  $\text{Na}^+$  channels responsible for the action potential than differences in the density of the persistent  $\text{Na}^+$  channels. Sensory fibers have slower fast  $\text{Na}^+$  channels (i.e., slowed  $\tau_m$ ) than motor fibers (Honmou et al. 1994), and this difference can alter both the chronaxie time and recovery cycle. Figure 5A shows that slowing  $\tau_m$  by 40% decreased the amplitude and duration of the supernormal period, and slowing  $\tau_m$  also resulted in a 20% increase in  $\tau_{\text{SD}}$ . Both of these effects of changing  $\tau_m$  match with the experimentally determined differences in the motor and sensory recovery cycle (Kiernan et al. 1996) and strength-duration relationship (Panizza et al. 1994) and were accomplished using an experimentally documented difference in  $\text{Na}^+$  channel kinetics.

Our simulation results have also identified the inactivation gate of the  $\text{Na}^+$  channel as an important factor influencing the recovery cycle. Experimental results from mammalian motor and sensory fibers show that sodium channel inactivation is faster in sensory fibers than in motor fibers (Mitrovic et al. 1993). Figure 5B shows that decreasing  $\tau_h$  by 20% resulted in a decrease in the duration and amplitude of the supernormal period, and decreasing  $\tau_h$  also decreased the action potential spike width. Both of these effects of changing  $\tau_h$  match with experimentally determined differences in the motor and sensory recovery cycle (Kiernan et al. 1996) and action potential spike shape (Kocsis et al. 1986) and were accomplished using an experimentally documented difference in  $\text{Na}^+$  channel kinetics. The alterations in  $\tau_m$  and  $\tau_h$  were not able to account for the differences in the subnormal period between motor and sensory fibers. The subnormal period is regulated by the slow  $\text{K}^+$  channel, and our results suggest that there is a difference in the density and/or distribution of these channels in motor and sensory fibers, with sensory fibers having a greater density of nodal and/or internodal slow  $\text{K}^+$  channels than motor fibers.

Another factor that could contribute to the differences between motor and sensory recovery cycles is the influence of fiber diameter on the amplitude of the super- and subnormal periods (Fig. 4B). Experimental measurements of the recovery cycle are traditionally made with extracellular electrodes placed on the arm (Kiernan et al. 1996). In such an arrangement, large-diameter fibers are activated at lower thresholds than small-diameter fibers (Fig. 7C). The fiber diameter distribution of the median nerve has more large-diameter sensory fibers ( $>14\text{-}\mu\text{m}$  fiber diam) than large-diameter motor fibers (Archibald et al. 1995). Therefore the sensory recovery cycle should have smaller super- and subnormal periods than the motor recovery cycle because larger diameter fibers have smaller super- and subnormal periods compared with smaller diameter fibers (Fig. 4B). Therefore differences in the morphological properties, as well as the dynamic properties of the ion channels, may contribute to the differences in the recovery cycle of motor and sensory fibers, and differences in the density of persistent  $\text{Na}^+$  channels may only be a second-order effect.

There is also variation between the recovery cycles of fibers

in different parts of the body (Lin et al. 2000). These variations may be correlated with changes in the DAP and AHP (and the underlying passive and active processes that regulate them) as seen in the studies of Barrett and Barrett (1982) and Bowe et al. (1987), where variability was recorded in the afterpotential amplitudes of different axons. The implication is that a given recovery cycle could reflect the function of a particular fiber type. Specifically, the recovery cycle could reflect slight biophysical or structural differences between fibers that influence their ability to propagate certain frequencies of input signals. These differences in activity-dependent excitability could act as a filter to optimize the performance of neurons for carrying specific information to synaptic targets or end-organs.

## APPENDIX

The ionic currents of the model can be written in the general form of

$$I_{\text{ion}} = g_{\text{ion}}(V_m - E_{\text{ion}})$$

where  $g_{\text{ion}}$  is the maximum conductance for the individual ion channel (Table 2) multiplied by gating variables that range from 0 to 1 (Hodgkin and Huxley 1952). The time and voltage dependence of each gating parameter ( $\omega$ ) is given by

$$\tau_{\omega} = 1/(\alpha_{\omega} + \beta_{\omega})$$

$$d\omega/dt = \alpha_{\omega}(1 - \omega) - \beta_{\omega}\omega$$

The time course and magnitude of the activation and inactivation parameters used in the simulations are given below. The maximum conductance density of the fast  $\text{Na}^+$  ( $g_{\text{Naf}}$ ), and slow  $\text{K}^+$  conductances ( $g_{\text{Ks}}$ ) were based on experimental single-channel conductance and channel density measurements. Based on the work of Scholz et al. (1993), a single-channel conductance of 15 and 8 pS were used for the fast  $\text{Na}^+$  and slow  $\text{K}^+$  channels, respectively. We used a density of 2,000 channels/ $\mu\text{m}^2$  (Waxman and Ritchie 1993) for the nodal fast  $\text{Na}^+$  channels, resulting in a  $g_{\text{Naf}}$  of 3.0 S/ $\text{cm}^2$ . We used a density of 100 channels/ $\mu\text{m}^2$  (Safronov et al. 1993) for the nodal slow  $\text{K}^+$  channels resulting in a  $g_{\text{Ks}}$  of 0.08 S/ $\text{cm}^2$ . The membrane dynamics were derived to be representative of neural excitation at 36°C. Alterations in the time constants of  $m$  or  $h$  were achieved by scaling both the  $\alpha$  and  $\beta$  components of the dynamical equations by the listed percentages. Individuals interested in reproducing the results of this study or using these models in their own work are encouraged to contact us for the appropriate NEURON files and instruction on their use.

### Fast sodium current

$$I_{\text{Naf}} = g_{\text{Naf}} * m^3 * h * (V_m - E_{\text{Na}})$$

$$\alpha_m = [6.57 * (V_m + 20.4)] / [1 - e^{-(V_m + 20.4)/10.3}]$$

$$\beta_m = \{0.304 * [-(V_m + 25.7)]\} / [1 - e^{[(V_m + 25.7)/9.16]}]$$

$$\alpha_h = \{0.34 * [-(V_m + 114)]\} / [1 - e^{[(V_m + 114)/11]}]$$

$$\beta_h = 12.6 / [1 + e^{-(V_m + 31.8)/13.4}]$$

### Persistent sodium current

$$I_{\text{Nap}} = g_{\text{Nap}} * p^3 * (V_m - E_{\text{Na}})$$

$$\alpha_p = [0.0353 * (V_m + 27)] / [1 - e^{-(V_m + 27)/10.2}]$$

$$\beta_p = \{0.000883 * [-(V_m + 34)]\} / [1 - e^{[(V_m + 34)/10]}]$$

### Slow potassium current

$$I_{\text{Ks}} = g_{\text{Ks}} * s * (V_m - E_{\text{K}})$$

$$\alpha_s = 0.3 / [1 + e^{[(V_m + 53)/-5]}]$$

$$\beta_s = 0.03 / [1 + e^{[(V_m + 90)/-1]}]$$

### Juxtaparanodal fast potassium current (used only in Fig. 9)

$$I_{\text{Kf}} = g_{\text{Kf}} * n^4 * (V_m - E_{\text{K}})$$

$$\alpha_n = [0.0462 * (V_m + 83.2)] / [1 - e^{-(V_m + 83.2)/1.1}]$$

$$\beta_n = \{0.0824 * [-(V_m + 66)]\} / [1 - e^{[(V_m + 66)/10.5]}]$$

### Leakage current

$$I_{\text{Lk}} = g_{\text{Lk}} * (V_m - E_{\text{Lk}})$$

This work was supported by National Science Foundation Grant BES-9709488, National Institutes of Health (NIH) Grant NS-40894, and NIH Training Fellowship HD-07500.

## REFERENCES

- ARCHIBALD SJ, SHEFNER J, KRARUP C, AND MADISON RD. Monkey median nerve repaired by nerve graft or collagen nerve guide tube. *J Neurosci* 15: 4109–4123, 1995.
- AWISZUS F. Effects of paranodal potassium permeability on repetitive activity of mammalian myelinated nerve fiber models. *Biol Cybern* 64: 69–76, 1990.
- AZOUZ R, JENSEN MS, AND YAARI Y. Ionic basis of spike after-depolarization and burst generation in adult rat hippocampal CA1 pyramidal cells. *J Physiol (Lond)* 492: 211–223, 1996.
- BAKER M, BOSTOCK H, GRAFE P, AND MARTIUS P. Function and distribution of three types of rectifying channel in rat spinal root myelinated axons. *J Physiol (Lond)* 383: 45–67, 1987.
- BARRETT EF AND BARRETT JN. Intracellular recording from vertebrate myelinated axons: mechanism of the depolarizing afterpotential. *J Physiol (Lond)* 323: 117–144, 1982.
- BARRETT EF, MORITA K, AND SCAPPATICCI KA. Effects of tetraethylammonium on the depolarizing after-potential and passive properties of lizard myelinated axons. *J Physiol (Lond)* 402: 65–78, 1988.
- BELEMENT SL AND RANCK JB. A quantitative study of electrical stimulation of central myelinated fibers. *Exp Neurol* 24: 147–170, 1969.
- BERGMANS J. *The Physiology of Single Human Nerve Fibres*. Vander, Belgium: University of Louvain, 1970.
- BERTHOLD CH, NILSSON I, AND RYDMARK M. Axon diameter and myelin sheath thickness in nerve fibres of the ventral spinal root of the seventh lumbar nerve of the adult and developing cat. *J Anat* 136: 483–508, 1983.
- BERTHOLD CH AND RYDMARK M. Electrophysiology and morphology of myelinated nerve fibers. VI. Anatomy of the paranode-node-paranode region in the cat. *Experientia* 39: 964–976, 1983.
- BLIGHT AR. Computer simulation of action potentials and afterpotentials in mammalian myelinated axons: the case for a lower resistance myelin sheath. *Neuroscience* 15: 13–31, 1985.
- BLIGHT AR AND SOMEYA S. Depolarizing afterpotentials in myelinated axons of mammalian spinal cord. *Neuroscience* 15: 1–12, 1985.
- BOSTOCK H, BAKER M, AND REID G. Changes in excitability of human motor axons underlying post-ischaemic fasciculations: evidence for two stable states. *J Physiol* 441: 537–557, 1991.
- BOSTOCK H AND BERGMANS J. Post-tetanic excitability changes and ectopic discharges in a human motor axon. *Brain* 117: 913–928, 1994.
- BOSTOCK H, CIKUREL K, AND BURKE D. Threshold tracking techniques in the study of human peripheral nerve. *Muscle Nerve* 21: 137–158, 1998.
- BOSTOCK H AND ROTHWELL JC. Latent addition in motor and sensory fibres of human peripheral nerve. *J Physiol (Lond)* 498: 277–294, 1997.
- BOSTOCK H AND SEARS TA. The internodal axon membrane: electrical excitability and continuous conduction in segmental demyelination. *J Physiol (Lond)* 280: 273–301, 1978.
- BOWE CM, KOCIS JD, AND WAXMAN SG. The association of the supernormal period and the depolarizing afterpotential in myelinated frog and rat sciatic nerve. *Neuroscience* 21: 585–593, 1987.



- BOYD IA AND KALU KU. Scaling factor relating conduction velocity and diameter for myelinated afferent nerve fibres in the cat hind limb. *J Physiol (Lond)* 289: 277–297, 1979.
- BURKE D, MOGYOROS I, VAGG R, AND KIERNAN MC. Quantitative description of the voltage dependence of axonal excitability in human cutaneous afferents. *Brain* 121: 1975–1983, 1998.
- CALDWELL JH, SCHALLER KL, LASHER RS, PELES E, AND LEVINSON SR. Sodium channel Na(v)1.6 is localized at nodes of ranvier, dendrites, and synapses. *Proc Natl Acad Sci USA* 97: 5616–5620, 2000.
- CHIU SY, RITCHIE JM, ROGART RB, AND STAGG D. A quantitative description of membrane currents in rabbit myelinated nerve. *J Physiol (Lond)* 292: 149–166, 1979.
- DAVID G, BARRETT JN, AND BARRETT EF. Activation of internodal potassium conductance in rat myelinated axons. *J Physiol (Lond)* 472: 177–202, 1993.
- DAVID G, MODNEY B, SCAPPATICCI KA, BARRETT JN, AND EF BARRETT. Electrical and morphological factors influencing the depolarizing afterpotential in rat and lizard myelinated axons. *J Physiol (Lond)* 489: 141–157, 1995.
- ENG DL, GORDON TR, KOCIS JD, AND WAXMAN SG. Development of 4-AP and TEA sensitivities in mammalian myelinated nerve fibers. *J Neurophysiol* 60: 2168–2179, 1988.
- FRANKENHAEUSER B AND HUXLEY AF. The action potential in the myelinated nerve fiber of *Xenopus laevis* as computed on the basis of voltage clamp data. *J Physiol (Lond)* 171: 302–315, 1964.
- GRILL WM. Modeling the effects of electric fields on nerve fibers: influence of tissue electrical properties. *IEEE Trans Biomed Eng* 46: 918–928, 1999.
- HALTER JA AND CLARK JW. A distributed-parameter model of the myelinated nerve fiber. *J Theor Biol* 148: 345–382, 1991.
- HALTER JA AND CLARK JW. The influence of nodal constriction on conduction velocity in myelinated nerve fibers. *Neuroreport* 4: 89–92, 1993.
- HINES ML AND CARNEVALE NT. The NEURON simulation environment. *Neural Comput* 9: 1179–1209, 1997.
- HODGKIN AL AND HUXLEY AF. A quantitative description of membrane current and its application to conduction and excitation in nerve. *J Physiol (Lond)* 117: 500–544, 1952.
- HONMOU O, UTZSCHNEIDER DA, RIZZO MA, BOWE CM, WAXMAN SG, AND KOCIS JD. Delayed depolarization and slow sodium currents in cutaneous afferents. *J Neurophysiol* 71: 1627–1637, 1994.
- HUXLEY AF AND STAMPFLI R. Evidence for saltatory conduction in peripheral myelinated nerve fibers. *J Physiol (Lond)* 108: 315–339, 1949.
- JACK JJ. Physiology of peripheral nerve fibres in relation to their size. *Br J Anaesth* 47: 173–182, 1975.
- KAPOOR R, SMITH KJ, FELTS PA, AND DAVIES M. Internodal potassium currents can generate ectopic impulses in mammalian myelinated axons. *Brain Res* 611: 165–169, 1993.
- KIERNAN MC, BURKE D, ANDERSEN KV, AND BOSTOCK H. Multiple measures of axonal excitability: a new approach in clinical testing. *Muscle Nerve* 23: 399–409, 2000.
- KIERNAN MC, MOGYOROS I, AND BURKE D. Differences in the recovery of excitability in sensory and motor axons of human median nerve. *Brain* 119: 1099–1105, 1996.
- KOCIS JD, BOWE CM, AND WAXMAN SG. Different effects of 4-aminopyridine on sensory and motor fibers: pathogenesis of paresthesias. *Neurology* 36: 117–120, 1986.
- LIN CS, MOGYOROS I, AND BURKE D. Recovery of excitability of cutaneous afferents in the median and sural nerves following activity. *Muscle Nerve* 23: 763–770, 2000.
- McINTYRE CC AND GRILL WM. Sensitivity analysis of a model of mammalian neural membrane. *Biol Cybern* 79: 29–37, 1998.
- MITROVIC N, QUASTHOFF S, AND GRAFE P. Sodium channel inactivation kinetics of rat sensory and motor nerve fibres and their modulation by glutathione. *Pflügers Arch* 425: 453–461, 1993.
- MOGYOROS I, KIERNAN MC, AND BURKE D. Strength-duration properties of human peripheral nerve. *Brain* 119: 439–447, 1996.
- NILSSON I AND BERTHOLD CH. Axon classes and internodal growth in the ventral spinal root L7 of adult and developing cats. *J Anat* 156: 71–96, 1988.
- PANIZZA M, NILSSON J, ROTH BJ, GRILL SE, DEMIRCI M, AND HALLETT M. Differences between the time constant of sensory and motor peripheral nerve fibers: further studies and considerations. *Muscle Nerve* 21: 48–54, 1998.
- PANIZZA M, NILSSON J, ROTH BJ, ROTHWELL J, AND HALLETT M. The time constants of motor and sensory peripheral nerve fibers measured with the method of latent addition. *Electroencephalogr Clin Neurophysiol* 93: 147–154, 1994.
- RANCK JB AND BeMENT SL. The specific impedance of the dorsal columns of cat: an anisotropic medium. *Exp Neurol* 11: 451–463, 1965.
- REID G, SCHOLZ A, BOSTOCK H, AND VOGEL W. Human axons contain at least five types of voltage-dependent potassium channel. *J Physiol (Lond)* 518: 681–696, 1999.
- RICHARDSON AG, McINTYRE CC, AND GRILL WM. Modeling the effects of electric fields on nerve fibres: influence of the myelin sheath. *Med Biol Eng Comput* 38: 438–446, 2000.
- ROBERTS WJ AND SMITH DO. Analysis of threshold currents during microstimulation of fibres in the spinal cord. *Acta Physiol Scand* 89: 384–394, 1973.
- ROPER J AND SCHWARZ JR. Heterogeneous distribution of fast and slow potassium channels in myelinated rat nerve fibres. *J Physiol* 416: 93–110, 1989.
- RYDMARK M. Nodal axon diameter correlates linearly with internodal axon diameter in spinal roots of the cat. *Neurosci Lett* 24: 247–250, 1981.
- RYDMARK M AND BERTHOLD CH. Electron microscopic serial section analysis of nodes of Ranvier in lumbar spinal roots of the cat: a morphometric study of nodal compartments in fibres of different sizes. *J Neurocytol* 12: 537–565, 1983.
- SAFRONOV BV, KAMPE K, AND VOGEL W. Single voltage-dependent potassium channels in rat peripheral nerve membrane. *J Physiol (Lond)* 460: 675–691, 1993.
- SCHOLZ A, REID G, VOGEL W, AND BOSTOCK H. Ion channels in human axons. *J Neurophysiol* 70: 1274–1279, 1993.
- SCHWARZ JR, REID G, AND BOSTOCK H. Action potentials and membrane currents in the human node of Ranvier. *Pflügers Arch* 430: 283–292, 1995.
- SMITH MR, SMITH RD, PLUMMER NW, MEISLER MH, AND GOLDIN AL. Functional analysis of the mouse Scn8a sodium channel. *J Neurosci* 18: 6093–6102, 1998.
- STEPANOVA DI AND BOSTOCK H. A distributed-parameter model of the myelinated human motor nerve fibre: temporal and spatial distributions of action potentials and ionic currents. *Biol Cybern* 73: 275–280, 1995.
- STYS PK AND ASHBY P. An automated technique for measuring the recovery cycle of human nerves. *Muscle Nerve* 13: 750–758, 1990.
- STYS PK, LEHNING E, SAUBERMANN AJ, AND LoPACHIN RM. Intracellular concentrations of major ions in rat myelinated axons and glia: calculations based on electron probe X-ray microanalyses. *J Neurochem* 68: 1920–1928, 1997.
- STYS PK, SONTHEIMER H, RANSOM BR, AND WAXMAN SG. Noninactivating tetrodotoxin-sensitive Na<sup>+</sup> conductance in rat optic nerve axons. *Proc Natl Acad Sci USA* 90: 6976–6980, 1993.
- STYS PK AND WAXMAN SG. Activity-dependent modulation of excitability: implications for axonal physiology and pathophysiology. *Muscle Nerve* 17: 969–974, 1994.
- TASAKI I. New measurements of the capacity and the resistance of the myelin sheath and nodal membrane of the isolated frog nerve fiber. *Am J Physiol* 181: 639–650, 1955.
- VABNICK I, TRIMMER JS, SCHWARZ TL, LEVINSON SR, RISAL D, AND SHRAGER P. Dynamic potassium channel distributions during axonal development prevent aberrant firing patterns. *J Neurosci* 19: 747–758, 1999.
- WARMAN EN, GRILL WM, AND DURAND D. Modeling the effects of electric fields on nerve fibers: determination of excitation thresholds. *IEEE Trans Biomed Eng* 39: 1244–1254, 1992.
- WASHBURN DL, ANDERSON JW, AND FERGUSON AV. A subthreshold persistent sodium current mediates bursting in rat subfornical organ neurones. *J Physiol (Lond)* 529: 359–371, 2000.
- WAXMAN SG. Determinants of conduction velocity in myelinated nerve fibers. *Muscle Nerve* 3: 141–150, 1980.
- WAXMAN SG AND RITCHIE JM. Molecular dissection of the myelinated axon. *Ann Neurol* 33: 121–136, 1993.
- YANG Q, KAJI R, HIROTA N, KOJIMA Y, TAKAGI T, KOHARA N, KIMURA J, SHIBASAKI H, AND BOSTOCK H. Effect of maturation on nerve excitability in an experimental model of threshold electrotonus. *Muscle Nerve* 23: 498–506, 2000.
- ZHOU L AND CHIU SY. Computer model for action potential propagation through branch point in myelinated nerves. *J Neurophysiol* 85: 197–210, 2001.
- ZHOU L, MESSING A, AND CHIU SY. Determinants of excitability at transition zones in Kv1.1-deficient myelinated nerves. *J Neurosci* 19: 5768–5781, 1999.